

Untangling dust emission and CIB anisotropies with the Scattering Transform Statistics

Srijita Sinha ^{*1}, Tuhin Ghosh ^{**1}, Erwan Allys², François Boulanger², Jean-Marc Delouis³

¹ National Institute of Science Education and Research, An OCC of Homi Bhabha National Institute, Bhubaneswar 752050, Odisha, India

² Laboratoire de Physique de l'École normale supérieure, ENS, Université PSL, CNRS, Sorbonne Université, Université Paris Cité, F-75005 Paris, France

³ Laboratoire d'Océanographie Physique et Spatiale (LOPS), Univ. Brest, CNRS, Ifremer, IRD, Brest, France

ABSTRACT

Context. Template-fit approach is often used to separate the Galactic dust emission and the cosmic infrared background (CIB) anisotropies at low H I column density regions with an underlying assumption that the gas and dust are tightly correlated. However, this method fails in regions where additional Galactic emission within the molecular hydrogen, diffuse ionized gas, and dark gas are present.

Aims. To develop and test a statistical component separation to extract the dust signal from the contaminated *Planck* 353 GHz observations using the Scattering Covariance (SC) statistics, which is a subclass of Scattering Transform statistics.

Methods. We first obtain a set CIB maps over 25 square patches, each with a sky area of 222 deg², using the linear correlation of dust and Galactic 21 cm H I emission valid at low H I column density regions using the template-fit approach. We then construct, from these 25 maps, a generative models of CIB using SC statistics. We finally rely on this contamination model to perform a component separation of dust and CIB in the *Planck* data for different sky regions. These separations are done using an algorithm that rely on a pixel-based optimization under joint SC-based losses, that constraint in particular the statistical correlation between the different astrophysical components.

Results. We validate our algorithm and separate the dust emission from the contamination in the *Planck* 353 GHz observations. We show the results of the recovered dust map for a test sky region where there is a significant difference between the *Planck* dust map and CSFD map. We find that the *Planck* dust map has more structures as compared to the CSFD map. We compare the power spectrum of the recovered dust map and $N_{\text{H I}}$ map and find a difference in slope ($\Delta\alpha \approx 0.4$) by fitting a power-law model to both the spectrum. To explain $\Delta\alpha$, we decompose the recovered dust map into two gas phases: dust associated with $N_{\text{H I}}$ and dust associated with N_{H_2} . This work provides a clear pathway to map the Galactic interstellar reddening over intermediate and high Galactic latitudes.

Key words. methods: statistical, ISM: dust, extinction, infrared: diffuse background, submillimeter: diffuse background

1. Introduction

The cosmic microwave background (CMB) signal encoding the history of the Universe at microwave and far-infrared frequencies is buried deep under the large-scale emission from the Galaxy and the small-scale emission from the extra-galactic sources (Ichiki 2014). At frequencies above 200 GHz, the diffuse thermal emission from our own Galaxy and the cosmic infrared background (CIB, Puget et al. 1996; Lagache et al. 2005) are the primary contributors to foreground emission (Planck 2018 results. IV. 2020). Galactic thermal dust emission provides a wealth of information regarding the complex physical systems that form the ISM (Draine 2011). The CIB is the diffuse radiation from dust particles in star-forming galaxies through the evolution of the Universe and acts as a probe for dark matter distribution and star formation history (Hauser & Dwek 2001; Planck 2013 results. XXX. 2014; Maniyar, A. S. et al. 2018). Moreover, CIB plays a vital role in de-lensing the observed CMB *B*-modes (Larsen et al. 2016). Although they have very different origins, dust emission and CIB share a similar spectral energy distribution; both follow a modified black-body law with

a slightly different spectral index. Separating these two components is challenging using only the spectral information.

Galactic thermal dust emission was observed to be tightly correlated with the 21 cm H I emission in low H I column density regions (Boulanger et al. 1996; Boulanger & Perault 1988). For this reason, the H I emission map is often used as a tracer of the dust emission within a template-fit approach to separate it from the CIB anisotropies (Planck intermediate results. XVII. 2014; Adak et al. 2024) and study its spectral energy distribution. Several other attempts have been made to obtain a clean map of CIB anisotropies by taking advantage of the full velocity coverage ($|v_{\text{LSR}}| < 600 \text{ km s}^{-1}$) of 21 cm H I observations (Planck early results. XXIV. 2011; Lenz et al. 2019; McCarthy 2024). The dust-CIB separation using the template-fit approach however becomes challenging when the zero-level of the sky background is unknown and there are significant variations in the dust emissivity at high Galactic latitudes. Planck 2013 results. VIII. (2014) has used a constant dust emissivity at very low H I column density regions ($N_{\text{H I}} < 2 \times 10^{20} \text{ cm}^{-2}$) to set the zero level of the *Planck* intensity map at 857 GHz. *Planck* 857 GHz was then used as a reference to set zero level of all other *Planck* HFI intensity maps. More recently, Adak et al. (2024) generalized this approach by fitting pixel-dependent dust emissiv-

* Corresponding author: sinha.srijita@niser.ac.in

** Corresponding author: tghosh@niser.ac.in

ity and a global offset using the Galactic H I template within a Bayesian inference framework. The separation between dust and CIB can be performed at the power spectrum level, where the N_{HI} power spectrum is used as a tracer of the dust power spectrum and subtracted from the total map to estimate the CIB power spectrum (Mak et al. 2017; Viero et al. 2019). Another model-independent approach used the Generalized Needlet Internal Linear Combination method that employs spatial information of the CIB in terms of its angular power spectrum to disentangle dust emission from CIB anisotropies (Planck intermediate results. XLVIII. 2016).

Another approach to separate dust emission from CIB anisotropies is to rely on Scattering Transform (ST) statistics. ST are a family of low-variance summary statistics inspired by neural networks that efficiently characterize non-Gaussian processes (Bruna & Mallat 2013; Andén & Mallat 2014). ST statistics are constructed from convolutions with a set of pass-band wavelets that separate a signal into its different scales, and nonlinear operations, such as modulus, that characterize the interaction, *i.e.*, the statistical dependency, between these different scales (Cheng & Ménard 2021). Since their introduction in astrophysics, these statistics have consistently approached or reached the state of the art in characterizing, classifying, and inferring parameters in various domains, such as the interstellar medium (Allys, E. et al. 2019; Regaldo-Saint Blancard, B. et al. 2020; Saydjari et al. 2021; Lei & Clark 2023; Richard et al. 2025), the large scale structures of the Universe (Allys et al. 2020; Eickenberg et al. 2022; Valogiannis & Dvorkin 2022), weak lensing (Cheng et al. 2020; Cheng & Ménard 2021), and the epoch of reionization (Greig et al. 2022; Hothi, Ian et al. 2024).

Additionally, scattering transforms offer the ability to construct an approximate generative model of a given process from an estimate of its ST statistics (Bruna & Mallat 2018). This has been demonstrated for various physical processes, with models sometimes constructed from a single image (Allys et al. 2020; Cheng et al. 2024). Initially developed for two-dimensional (2D) planar data, these models have since been expanded to include multi-frequency data (Blancard et al. 2023), spherical data (Mousset et al. 2024; Campeti et al. 2025), and even spectroscopic data (Hothi et al. 2026). Regarding CMB studies, simulated data has shown that a ST generative model constructed from a single dust foreground patch can suffice to train a neural network to distinguish primordial B-modes from dust emission, even within a challenging mono-frequency approach (Jefrey et al. 2021).

Moreover, new ST-based component separation algorithms have been developed. Introduced in Regaldo-Saint Blancard, Bruno et al. (2021); Delouis, J.-M. et al. (2022) to separate Galactic dust emission from instrumental noise in *Planck* data, these versatile algorithms relied on pixel-space optimization under ST statistics constraints to generate dust maps compatible with the data once added to the noise. In these paper, the ability of these algorithms to leverage the different non-Gaussian properties of different signals is emphasized by the fact that the separations are performed at a single frequency. Additionally, these separations were performed without assuming a prior model of the component of interest, dust in this case. Recently, Auclair, Constant et al. (2024) used an ST-based algorithm to separate dust emission from CIB anisotropies in *Herschel* SPIRE observations. A major success of this paper is that this separation was achieved by relying only on observational data, first learning an ST-based CIB model from a sky region where this signal was dominant, and then using this model to separate Galactic dust

emission and CIB in the Spider region. More recently, Tsouros et al. (2026) used the ST-based component separation to recover the polarized dust emission from the *Planck* data at 353 GHz.

The main goal of this paper is to build on previous work and separate the Galactic dust emission in *Planck* 353 GHz data from the CIB anisotropies and instrumental noise. To do so, we first construct a ST-based contamination model of CIB and instrumental noise over a set of square patches, each with a sky area of 222 deg^2 , in regions of low H I column density. Secondly, we use this contamination model to perform a ST-based component separation in regions of intermediate H I column densities. We use the particular Scattering Covariance (SC) statistics, a sub-class of the ST statistics for this work. We work with *Planck* 353 GHz data smoothed to $16.2'$ (FWHM) beam resolution to match the resolution of the H I emission maps. At this beam resolution, the CIB anisotropies dominates over instrumental noise. Before applying the component separation algorithm to the real *Planck* data, we successfully test it on the simulated *Planck* maps with different signal-to-noise ratios (SNRs) of the dust emission with respect to the contamination.

The paper is organised as follows. In Sect. 2, we describe the *Planck* data and the external datasets (HI4PI and CSFD dust reddening map) used in our study. Section 3 describes briefly the results of the template-fit approach to get the contamination map (or dust-subtracted *Planck* map) at 353 GHz over the low H I column density regions ($N_{\text{HI}} < 4 \times 10^{20} \text{ cm}^{-2}$). In Sect. 4, we estimate the statistical properties of the contamination map from a limited set of square patches and its sample variance. In Sect. 5, we briefly present the set of ST statistics used in the paper. The component separation algorithm using the ST statistics is described in Sect. 6. In Sect. 7, we apply our algorithm on *Planck* simulations at 353 GHz. We present and discuss the results of the dust-CIB separation obtained from the *Planck* 353 GHz observations in Sect. 8, and finally we summarise our findings in Sect. 9.

2. Data Sets

2.1. *Planck* data

We use the publicly available SMICA CMB-subtracted intensity map from the *Planck* legacy data release¹ (PR3) at 353 GHz (Planck 2018 results. I. 2020). The 353 GHz map is provided in HEALPix² (Górski et al. 2005) format at $N_{\text{side}} = 2048$ (pixel size $\sim 1.7'$) with an angular beam resolution of $4.82'$ FWHM (Planck 2018 results. III. 2020; Planck 2018 results. IV. 2020). We then smooth the map at a beam resolution of $16.2'$ (by convolving it with an additional Gaussian beam of $\sqrt{(16.2')^2 - (4.82')^2} = 15.47'$) and downgrade it to $N_{\text{side}} = 512$ (pixel size $6.8'$). We convert the map from K_{CMB} to kJy sr^{-1} units using the conversion factors given in Planck 2013 results. IX. (2014). We retain the CIB monopole that was added by hand to the *Planck* data at 353 GHz. From the HEALPix map, we extract 2D tangential projection square patches (256×256 pixels) centered around HEALPix pixel of $N_{\text{side}} = 4$ using the reproject python package (Robitaille et al. 2020). The pixel size for each square patch is $3.5'$, resulting in a total patch area of 222 deg^2 .

We use the end-to-end Full Focal Plane 10 (FFP10) noise simulations at 353 GHz (Planck 2015 results - XII. 2016) to estimate the variance of the instrumental noise present in the *Planck* 353 GHz data. Similar to the *Planck* data, we first smooth

¹ <http://pla.esac.esa.int/pla>

² <http://healpix.sf.net>

the noise maps with an additional Gaussian beam smoothing of $15.47'$, reproject them to $N_{\text{side}} = 512$ and then we extract the 2D patches from them.

2.2. External datasets

We use the HI4PI full-sky map with a spectral resolution of 1.49 km s^{-1} , which combines the data from the Effelsberg-Bonn HI Survey (EBHIS; Winkel, B. et al. 2016) and the Galactic All-Sky Survey (GASS; McClure-Griffiths et al. 2009; Kalberla et al. 2010). The map is provided on the HEALPix grid at $N_{\text{side}} = 1024$ (pixel size $3.4'$) and a common angular beam resolution of $16.2'$ (FWHM). The root mean square brightness temperature uncertainty is 43 mK . Along the optically thin line-of-sight, the total HI column density (N_{HI} , in units of 10^{18} cm^{-2}) can be obtained by integrating the brightness temperature (T_b) over the velocity channels (v) using the relation (Dickey & Lockman 1990):

$$N_{\text{HI}} = 1.82 \int T_b dv \text{ cm}^{-2}. \quad (1)$$

Following Hayakawa & Fukui (2024), we integrate the HI column density over two velocity ranges: one with low-velocity (LV, $|v_{\text{LSR}}| < 30 \text{ km s}^{-1}$) and the other with intermediate-velocity (IV, $30 \text{ km s}^{-1} < |v_{\text{LSR}}| < 90 \text{ km s}^{-1}$). In this study, we ignore the high-velocity HI emission (HV, $|v_{\text{LSR}}| > 90 \text{ km s}^{-1}$) as no significant dust emission is associated with the HV template (Wakker & Boulanger 1986; Planck early results. XXIV. 2011; Lenz et al. 2016; Hayakawa & Fukui 2024). Finally, we downgrade the LV and IV HI emission maps to the HEALPix grid of $N_{\text{side}} = 512$ and extract 2D square patches centered around HEALPix pixel of $N_{\text{side}} = 4$. We treat the two HI emission maps as the tracers of the dust emission. We use the sum of IV and LV HI column densities as a measure of total HI column density (N_{HI}).

The all-sky Galactic dust reddening map produced by Schlegel, Finkbeiner, & Davis (1998, hereafter SFD) at $100 \mu\text{m}$ has imprints of extragalactic large-scale structure (LSS) or CIB (Chiang & Ménard 2019). The CIB map at $100 \mu\text{m}$ is reconstructed by cross-correlating the SFD map with the spectroscopic galaxies and quasars in SDSS. The Corrected SFD (CSFD) is produced by subtracting the CIB contamination from the SFD map³ (Chiang 2023). We work with both CSFD map and LSS map at $N_{\text{side}} = 512$ and smoothed at a common beam resolution of $16.2'$ (FWHM). The CSFD map is used as a tracer for the dust emission to produce the *Planck* simulations.

3. Contamination map from template-fit approach

In this section, we briefly discuss how we obtain the contamination map (or dust-subtracted *Planck* map) at 353 GHz . We use Adak et al. (2024) formalism to fit pixel-dependent dust emissivity and a global offset over low N_{HI} regions ($N_{\text{HI}} < 4 \times 10^{20} \text{ cm}^{-2}$) using the template-fit approach. We use LV and IV HI templates as a tracer the dust emission. As both LV and IV maps are the full-sky maps, we can easily include both northern and southern Galactic hemispheres in the analysis, and hence increase the total sky coverage.

We follow the iterative correlation methodology of Planck intermediate results. XVII. (2014) to construct a global mask, which is defined as follows. Over the initial mask with $N_{\text{HI}} < 4 \times 10^{20} \text{ cm}^{-2}$, we compute the pixel-dependent dust emissivity between the CMB-subtracted *Planck* intensity map at 353 GHz

and the two HI templates, and then subtract the best-fit model from the *Planck* 353 GHz data to produce a residual map. We fit a Gaussian to the residuals, calculate its standard deviation (σ_G) and remove pixels that have absolute values greater than $5\sigma_G$. We repeat the same procedure until all pixels in the residual map fall within $5\sigma_G$ region of the Gaussian fit to the residuals. In our case, we arrive at a converged Galactic mask after five iterations, covering a region of $\sim 13800 \text{ deg}^2$. The total sky fraction covered by the unmasked pixels is $f_{\text{sky}} = 0.33$.

We model the input CMB-subtracted *Planck* intensity data (m) at 353 GHz as the sum of the dust emission (s), CIB anisotropies (c), and the instrumental noise (n):

$$m = s + c + n. \quad (2)$$

The global offset of the map (including the CIB monopole) term is included in the signal term s . Using Adak et al. (2024) formalism, we sample the joint probability distribution of pixel-dependent dust emissivity and the global offset given the two HI templates and the input data. The contributions of CIB anisotropies and instrumental noise are propagated through the noise covariance matrix (Adak et al. 2024).

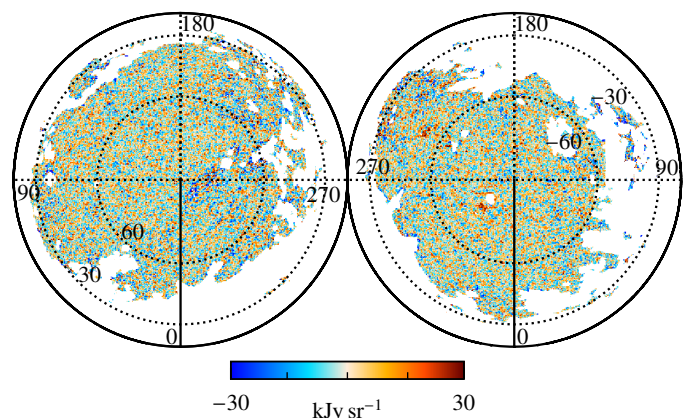


Fig. 1. Orthographic projection of the residual map obtained from the template-fit approach. The northern (southern) Galactic hemisphere is on the left (right). White regions are masked from the analysis as it comprises of N_{HI} cut-off pixels and the pixels masked due to iterative masking.

We refer to the dust map estimated from the template-fit approach within the Bayesian inference framework as s_B . Next, we subtract s_B from the input CMB-subtracted map to obtain the residual map, $r_B = m - s_B$, which includes the CIB anisotropies, instrumental noise, and possible residual dust emissions (not correlated with the two HI templates). The global offset term (including the CIB monopole term) is included in s_B . We report a global offset value of $119.2 \pm 0.2 \text{ kJy sr}^{-1}$ over the Galactic mask used in our analysis. Our value is very close to the CIB monopole of 120 kJy sr^{-1} added to the *Planck* map at 353 GHz based on the Béthermin, M. et al. (2010) CIB model. The expected standard deviation of instrumental noise from FFP10 simulations over the Galactic mask is 3.3 kJy sr^{-1} , whereas the expected standard deviation of the CIB anisotropies based on the *Planck* 2013 best-fit CIB model (Planck 2013 results. XXX. 2014) is 9.3 kJy sr^{-1} . Because the standard deviation of two uncorrelated components is added in quadrature, we can safely assume that r_B map is dominated by the CIB anisotropies. The residual map at 353 GHz over the Galactic mask is shown in Fig. 1 in orthographic projection.

³ <https://doi.org/10.5281/zenodo.8207175>

4. Statistical properties of the residual map over square patches

For our purpose, we first extract 48 square patches (24 in the northern and 24 in the southern Galactic hemisphere) of size $14.9^\circ \times 14.9^\circ$ (sky area of 222 deg^2) centered around the center of $N_{\text{side}} = 4$ HEALPix grid pixels at the high Galactic latitudes ($|b| > 45^\circ$). The pixel resolution of each square patch is $3.5'$ and contains 256×256 pixels. We note that $N_{\text{side}} = 4$ pixels have a pixel size of $14.7^\circ \times 14.7^\circ$. All the square patches have very minimal overlap and hence provide independent measurement of the statistical properties of the residual map at 353 GHz. Out of these 48 square patches, we select only 25 square patches that are not severely affected by the initial mask to select the low N_{HI} regions and the pixels that are masked due to the iterative masking algorithm discussed in Sect. 3. Out of all 25 square patches, 17 square patches that are completely unaffected by the final mask. Only few pixels in the remaining 8 square patches are slightly affected by the final mask. The percentage of these masked pixels in those patches is less than 1.5%. For these 25 square patches, SNR defined as $\sigma_{s_B}/\sigma_{r_B}$ varies from 1 to 2.9.

To avoid any bias in the computation of the statistical properties of the residual map, we further identify the pixels whose values deviate more than $\pm 3\sigma_{r_B}$ and inpaint them using linear interpolation with `griddata` function from `scipy.interpolate` package (Virtanen et al. 2020). Finally, the inpainted patches have no pixels deviating $\pm 3\sigma_{r_B}$. Figure 2 presents all the patches after inpainting used to derive the statistical properties of the residual map. All the patches follow Gaussian distribution with a mean standard deviation (σ_{r_B}) of 8.9 kJy sr^{-1} . The estimated standard deviation of σ_{r_B} from these patches is 0.4 kJy sr^{-1} , which is much smaller than its mean value. This shows that there is no significant outlier patch is included in the analysis. We compute the power spectrum (C_ℓ) in these patches us-

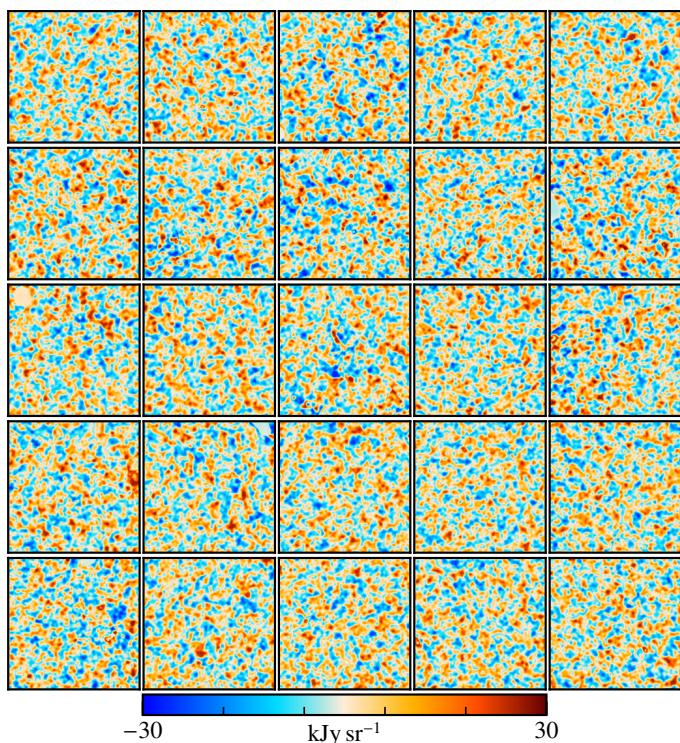


Fig. 2. The spatial distribution of the residual maps in the selected 25 square patches.

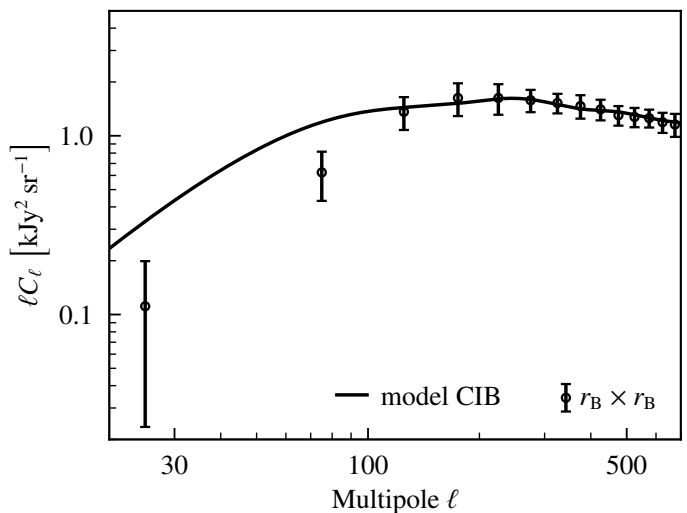


Fig. 3. The black points show the average power spectrum, in terms of ℓC_ℓ , with multipole ℓ over all the 25 selected square patches. The error bars on them are the standard deviation obtained on the spectra. The black solid line represents Lenz et al. (2019) best-fit CIB model at 353 GHz.

ing the discrete Fourier transform in the flat sky approximation (Hivon et al. 2002), implemented in the publicly-available package NaMaster⁴(Alonso et al. 2019). As these patches do not obey periodic boundary conditions, we mask the boundary pixels in the computation of the power spectrum. We first make a binary mask considering only 180×180 inner pixels as shown in the left panel of Fig. A.1. We then taper the boundary with a cosine function to make the apodised mask (see right panel of Fig. A.1). The errors on the power spectrum are computed from the analytic Gaussian covariance matrix using NaMaster. We correct for the final power spectrum for the beam effect and the pixel window effect.

The average power spectrum of these patches are shown in Fig. 3. The sample variance of the power spectrum between all the patches agrees well with each other and broadly consistent with the Lenz et al. (2019) best-fit CIB model (shown with a thick solid black line). At higher multipoles $\ell > 100$, we find a very good match between our measurements of average power spectrum of the residuals and the Lenz et al. (2019) CIB model. It shows that the contamination by the Galactic residuals containing the dust emission from H_2 gas or ionized hydrogen is negligible in our 25 selected square patches. We show the average power spectrum upto $\ell_{\text{max}} = 700$, as the higher multipoles are significantly affected by the beam correction.

We compute the Minkowski functionals (MF) for these patches. The MFs provide insight into the geometrical and topological structures of these regions as a variation of pixel threshold value. For a 2D square patch, the MFs are the area (\mathcal{V}_0), perimeter (\mathcal{V}_1) and the Euler characteristic of the connected pixels and the number of holes in the same space or Genus (\mathcal{V}_2). We use the publicly available QuantImpy package (Mantz et al. 2008; Boelens & Tchlepi 2021) to compute the MFs in these regions. Figure 4 shows that the MFs of all the 25 selected square patches. We use Lenz et al. (2019) best-fit CIB model to generate 10 Gaussian realization of CIB map and add 10 FFP10 noise realizations to it for a given patch. The black solid line in Fig. 4 is the mean MFs obtained from the Gaussian CIB and non-Gaussian FFP10 noise realization. As the instrumental noise is

⁴ <https://github.com/LSSTDESC/NaMaster>

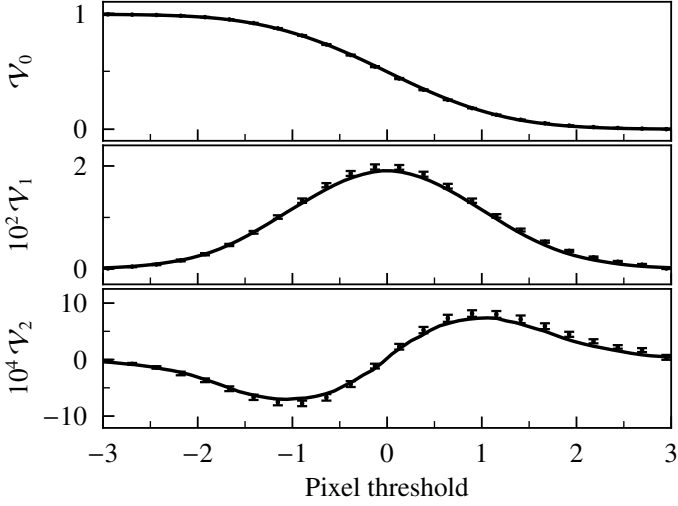


Fig. 4. The variation of \mathcal{V}_0 , \mathcal{V}_1 and \mathcal{V}_2 with pixel threshold of the Minkowski functionals over all the 25 patches. The perimeter and Euler functions are scaled with 10^2 and 10^4 respectively for visualisation purpose. The black solid line represents the MFs computed from the average of 10 Gaussian CIB realisations and 10 FFP10 noise realisations over a given patch.

subdominant at the chosen beam resolution of our analysis, we can conclude that the MFs of the 25 selected square patches follow closely the expected distribution from a Gaussian random field.

5. Scattering Covariance statistics

In this work, we use the SC statistics introduced in Cheng et al. (2024) and Mousset et al. (2024). The SC statistics correspond to the covariances of terms constructed from a combination of convolutions of the input random field X with a set of pre-calculated wavelets, as well as a non-linear modulus. SC statistics also include the L1 and L2 norms of these wavelet convolutions. The complex valued Morlet wavelet filters that we use, noted $\psi^{j,\gamma}$, are localised both in pixel and harmonic space, and are characterised by a dyadic scale j and an orientation γ . There are four types of SC statistics. The first S_1 and S_2 statistics characterize jointly the amplitude and sparsity of the process X at a single oriented scale $\lambda = (j, \gamma)$. The higher order wavelet moment estimators (S_3 and S_4) capture the interactions between two and three different oriented scales.

Auto- and cross-ST statistics can be computed between two random fields X and Y . The cross SC statistics are defined as

$$\begin{aligned} S_1^{\times,\lambda_1}(X, Y) &= \left\langle \left| (X * \psi^{\lambda_1})(Y * \psi^{\lambda_1})^* \right| \right\rangle, \\ S_2^{\times,\lambda_1}(X, Y) &= \left\langle (X * \psi^{\lambda_1})(Y * \psi^{\lambda_1})^* \right\rangle, \\ S_3^{\times,\lambda_1,\lambda_2}(X, Y) &= \text{Cov}(X * \psi^{\lambda_1}, |Y * \psi^{\lambda_2}| * \psi^{\lambda_1}), \\ S_{3p}^{\times,\lambda_1,\lambda_2}(X, Y) &= \text{Cov}(Y * \psi^{\lambda_1}, |X * \psi^{\lambda_2}| * \psi^{\lambda_1}), \\ S_4^{\times,\lambda_1,\lambda_2,\lambda_3}(X, Y) &= \text{Cov}(|X * \psi^{\lambda_3}| * \psi^{\lambda_1}, |Y * \psi^{\lambda_2}| * \psi^{\lambda_1}), \end{aligned} \quad (3)$$

where $*$ stands for a convolution, $\langle \cdot \rangle$ is the spatial average over the fields, and $\text{Cov}(X, Y)$ is the estimated covariances of X and Y . For auto-SC statistics, S_1 and S_2 are simplified to:

$$S_1^{\lambda_1}(X) = \left\langle |X * \psi^{\lambda_1}| \right\rangle, \quad \text{and} \quad S_2^{\lambda_1}(X) = \left\langle |X * \psi^{\lambda_1}|^2 \right\rangle \quad (4)$$

while S_3 and S_4 are obtained by setting $X = Y$ in the previous equations, and the redundant S_{3p} terms is removed. Following previous work (Cheng et al. 2024; Mousset et al. 2024; Campeti et al. 2025), we normalise the $S_3^{\times}(X, Y)$ and $S_4^{\times}(X, Y)$ coefficients by their own $S_2^{\times}(X, Y)$ statistics:

$$\bar{S}_3^{\times,\lambda_1,\lambda_2} = \frac{S_3^{\times,\lambda_1,\lambda_2}}{\sqrt{S_2^{\times,\lambda_1} S_2^{\times,\lambda_2}}}, \quad \text{and} \quad \bar{S}_4^{\times,\lambda_1,\lambda_2,\lambda_3} = \frac{S_4^{\times,\lambda_1,\lambda_2,\lambda_3}}{\sqrt{S_2^{\times,\lambda_2} S_2^{\times,\lambda_3}}}. \quad (5)$$

As we work with fields with 256×256 pixels, we probe $J = 5$ different wavelet scales with $j \in [0, J - 1]$ and a total of $L = 4$ orientations, considering a wavelet filter kernel with 5×5 pixels. With these values J and L , we obtain 2522 auto statistics and 2762 cross statistics. At the end, the final summary statistics Φ that we use for the cross statistics are the concatenation of the mean of the fields $\langle XY \rangle$, its variance $\text{Var}(XY)$, and normalised cross SC statistics, as

$$\Phi(XY) = \{ \langle XY \rangle, \text{Var}(XY), S_1^{\times,\lambda_1}, S_2^{\times,\lambda_1}, \bar{S}_3^{\times,\lambda_1,\lambda_2}, \bar{S}_{3p}^{\times,\lambda_1,\lambda_2}, \bar{S}_4^{\times,\lambda_1,\lambda_2,\lambda_3} \}. \quad (6)$$

and for the auto statistics the final summary statistics Φ are the concatenation of the mean of the field $\langle X \rangle$, its variance $\text{Var}(X)$ and normalised SC statistics, yielding:

$$\Phi(X) = \{ \langle X \rangle, \text{Var}(X), S_1^{\lambda_1}, S_2^{\lambda_1}, \bar{S}_3^{\lambda_1,\lambda_2}, \bar{S}_4^{\lambda_1,\lambda_2,\lambda_3} \}. \quad (7)$$

We compute these summary statistics using the python package Foscat⁵ (Delouis, J.-M. et al. 2022; Campeti et al. 2025).

6. Component separation algorithm

In this section, we present the component separation algorithm based on SC statistics to statistically separate the dust emission from the contamination at 353 GHz *Planck* observations.

6.1. Generative contamination maps

We generate 300 synthetic contamination maps (r_{syn}) from the 25 selected patches obtained in Sect. 4. These synthetic maps are constructed using maximum entropy generative models conditioned by the Φ statistics as defined in Eq. (7). We refer the reader to Bruna & Mallat (2018); Cheng et al. (2024); Mousset et al. (2024) for more details.

Here we discuss the steps that we follow to generate one of synthetic contamination maps. Starting from a white noise realization u_0 , we perform a gradient decent in pixel space to minimize the following⁶ loss function:

$$\mathcal{L}(u) = \|\Phi(r_B) - \Phi(u)\|^2, \quad (8)$$

where $\|\cdot\|$ is the Euclidean norm, and r_B is one of the residual patch. The samples of the generative models are the maps $r_{\text{syn},i}$ obtained at the end of the optimization, which verify:

$$\Phi(r_B) \approx \Phi(r_{\text{syn},i}). \quad (9)$$

We optimise the loss function using the gradient-descent algorithm in pixel space implemented in the Foscat package. The optimisation stops when the difference of the loss functions in the two consecutive iterations is less than 10^{-6} .

⁵ <https://github.com/jmdelouis/FOSCAT>

⁶ In addition to the normalization of the SC statistics described Eq. (5), we take here the log of the S_1 and S_2 coefficients.

6.2. Component separation algorithm

We start with the data map m which we aim to separate into the dust emission and the contamination. This is done by constructing maps that verify an ensemble of constraints which are constructed directly from the available data. The formalism for this statistical component separation closely follows the ones presented in [Delouis, J.-M. et al. \(2022\)](#) and [Auclair, Constant et al. \(2024\)](#). In our work, we use six constraints to recover a dust map statistically compatible with the information available in the *Planck* data. The algorithm relies on a gradient descent on a running u map, which corresponds, at the end of the optimization, to the recovered \tilde{s} map of the dust emission. We write below the constraints that this \tilde{s} map should fulfill, before expressing these constraints as losses involving the running u map. The first constraint ensures that the recovered signal added to the contamination statistically matches with the data. In terms of the summary statistics, the constraint is written as

$$\Phi(m) \simeq \left\langle \Phi(\tilde{s} + r_{\text{syn},i}) \right\rangle_{i \in N}, \quad (10)$$

where $\langle \cdot \rangle_i$ is the ensemble average over the N r_{syn} maps obtained in Sect. 6.1. The second constraint imposes that the cross-correlation between the data and the signal is conserved,

$$\Phi(m, \tilde{s}) \simeq \left\langle \Phi(\tilde{s} + r_{\text{syn},i}, \tilde{s}) \right\rangle_{i \in N}. \quad (11)$$

The third constraint imposes that the statistics of the residual map $\tilde{r} = (m - \tilde{s})$ should match those of the r_{syn} . This constraint ensures minimum leakage of the contamination into the recovered dust map. Mathematically,

$$\Phi(m - \tilde{s}) \simeq \left\langle \Phi(r_{\text{syn},i}) \right\rangle_{i \in N}, \quad (12)$$

The fourth constraint enforces that the recovered dust map retains the same correlation with the total N_{H1} map as present in the data. The assumption here is that the contamination maps, being independent to total N_{H1} , can be sampled again without modifying the estimate of the cross-statistics. Mathematically, it is written as

$$\Phi(N_{\text{H1}}, m) \simeq \left\langle \Phi(N_{\text{H1}}, \tilde{s} + r_{\text{syn},i}) \right\rangle_{i \in N}. \quad (13)$$

The fifth constraint is that the residual map is uncorrelated with the N_{H1} map, which yields,

$$\Phi(N_{\text{H1}}, m - \tilde{s}) \simeq \left\langle \Phi(N_{\text{H1}}, r_{\text{syn},i}) \right\rangle_{i \in N}. \quad (14)$$

Finally, the sixth constraint imposes that the residual map is uncorrelated with the dust map separately,

$$\Phi(\tilde{s}, m - \tilde{s}) \simeq \left\langle \Phi(\tilde{s}, r_{\text{syn},i}) \right\rangle_{i \in N}. \quad (15)$$

The last four constraints enforce minimal leakage of the dust signal into the contamination map at those angular scales at which the amplitude of the dust signal is comparable to that of the contamination.

Following [Delouis, J.-M. et al. \(2022\)](#), the mathematical loss functions corresponding to these constraints are respectively

written as:

$$\begin{aligned} \mathcal{L}_1(u) &= \left\| \frac{\Phi(m) - \Phi(u) - B_1}{\sigma_{\Phi(u+r_{\text{syn},i})}} \right\|^2, \\ B_1 &= \left\langle \Phi(u + r_{\text{syn},i}) - \Phi(u) \right\rangle_{i \in N} \\ \mathcal{L}_2(u) &= \left\| \frac{\Phi(m, u) - \Phi(u, u) - B_2}{\sigma_{\Phi(u+r_{\text{syn},i}, u)}} \right\|^2, \\ B_2 &= \left\langle \Phi(u + r_{\text{syn},i}, u) - \Phi(u, u) \right\rangle_{i \in N}, \\ \mathcal{L}_3(u) &= \left\| \frac{\Phi(m - u) - \left\langle \Phi(r_{\text{syn},i}) \right\rangle_{i \in N}}{\sigma_{\Phi(r_{\text{syn},i})}} \right\|^2, \\ \mathcal{L}_4(u) &= \left\| \frac{\Phi(N_{\text{H1}}, m) - \Phi(N_{\text{H1}}, u) - B_4}{\sigma_{\Phi(N_{\text{H1}}, u+r_{\text{syn},i})}} \right\|^2, \\ B_4 &= \left\langle \Phi(N_{\text{H1}}, u + r_{\text{syn},i}) - \Phi(N_{\text{H1}}, u) \right\rangle_{i \in N}, \\ \mathcal{L}_5(u) &= \left\| \frac{\Phi(N_{\text{H1}}, m - u) - \left\langle \Phi(N_{\text{H1}}, r_{\text{syn},i}) \right\rangle_{i \in N}}{\sigma_{\Phi(N_{\text{H1}}, r_{\text{syn},i})}} \right\|^2, \\ \mathcal{L}_6(u) &= \left\| \frac{\Phi(u, m - u) - \left\langle \Phi(u, r_{\text{syn},i}) \right\rangle_{i \in N}}{\sigma_{\Phi(u, r_{\text{syn},i})}} \right\|^2. \end{aligned} \quad (16)$$

We minimise the total loss function given as,

$$\mathcal{L}(u) = \mathcal{L}_1(u) + \mathcal{L}_2(u) + \mathcal{L}_3(u) + \mathcal{L}_4(u) + \mathcal{L}_5(u) + \mathcal{L}_6(u). \quad (17)$$

For a detailed concept behind the bias B and standard deviation σ we refer to [Delouis, J.-M. et al. \(2022\)](#). For example, the loss \mathcal{L}_1 is computed as the normalised chi-square distribution between $\Phi(m)$ and $\left\langle \Phi(u + r_{\text{syn},i}) \right\rangle_{i \in N}$. However, to allow for computational efficiency, it relies on an bias B_1 , which is estimated only after a certain number of iterations. This avoid the need to trace $\left\langle \Phi(u + r_{\text{syn},i}) \right\rangle_{i \in N}$ throughout the optimization. This bias is only necessary when the loss involve an ensemble average over the $r_{\text{syn},i}$ maps.

The different initial condition maps for the gradient descent are made from the m map smoothed with a W' (FWHM) Gaussian beam, where W is chosen randomly from a uniform distribution $\mathcal{U}[100, 200]$. Starting from one the initial map u_0 , we minimise the total loss function using the gradient-descent algorithm in *Foscat*. The final final dust map \tilde{s} correspond to u at the end of the optimisation, and the residual map is obtained as $\tilde{r} = (m - \tilde{s})$. In practice, we update the B_1 and B_2 biases and all variance terms every 150 iterations. We run this optimisation until the difference between two consecutive losses in an epoch is $\Delta\mathcal{L} < 0.002$. The typical number of epochs required to reach the $\Delta\mathcal{L}$ varies from 5 to 8 depending on the data map. Numerically, we found that decreasing $\Delta\mathcal{L}$ beyond 0.002 does not improve the recovered dust map. The total computation time ranges from 15 to 20 minutes on a single-node GPU cluster (NVIDIA A30), depending on the number of iterations performed.

7. Planck Simulations

We first validate the component separation algorithm described in Sect. 6.2 on simulated *Planck* maps on a 2D square patch.

7.1. Synthetic Contamination Maps

We synthesise 12 statistically identical realisations from each sky patch considered in Sect. 3, totaling $N = 300$ realisations

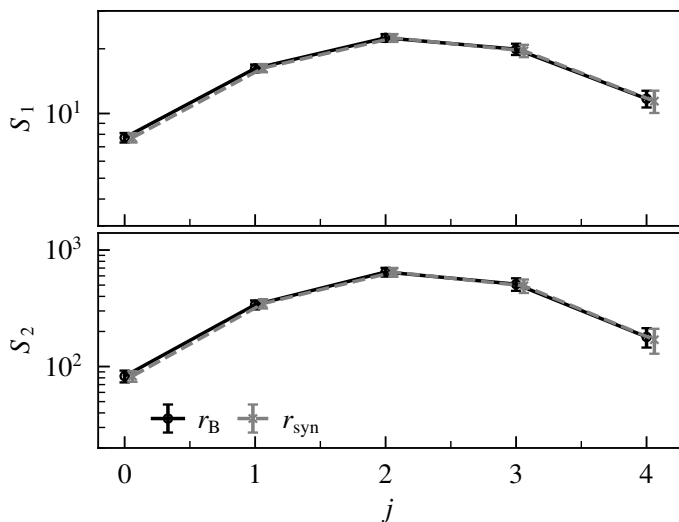


Fig. 5. Comparison of S_1 and S_2 statistics of mean and standard deviation of 25 contamination maps obtained from the template-fit approach r_B regions (black circles) and 300 synthetic contamination maps r_{syn} (gray crosses). The gray crosses are shifted in the x -axis.

of r_{syn} maps using the summary statistics as discussed in Sect. 6.1. The synthetic contamination maps retain all the statistical properties of the r_B and have a mean standard deviation $\sigma_{r_{\text{syn}}}$ of 9.0 kJy sr^{-1} and the estimated 1σ variation in the $\sigma_{r_{\text{syn}}}$ is 0.4 kJy sr^{-1} . These synthetic maps follow the Gaussian distribution and have the same one-dimensional probability distribution function as the r_B maps. We also compute the angular power spectra and the three MFs and see that they follow the mean r_B statistics. For brevity, we only show the mean and standard deviation of the S_1 and S_2 coefficients obtained from the 25 r_B and 300 r_{syn} maps in Fig. 5. We use these 300 r_{syn} maps to compute the variance on its summary statistics.

7.2. Simulated map at 353 GHz

We chose a test patch centered at Galactic coordinates $(l, b) = (45.0^\circ, -54.3^\circ)$ of sky area 222 deg^2 . The mean H I column density over the entire patch is $\langle N_{\text{H I}} \rangle = 3.3 \times 10^{20} \text{ cm}^{-2}$. We extract the same sky patch from the CSFD map and scale it with a constant factor to produce an input dust map. In our case, we kept the contamination map fixed and vary the dust amplitude to produce different SNR maps. The constant scaling factor controls the $SNRs$ of the input dust map with respect to the contamination.

We validate our algorithm for SNR 3 to 9. We discuss the $SNR = 3$ results in detail and highlight the primary differences among the others. We call the scaled 2D input dust map as s_{sim} , to which we add a realization of the contamination map (r_{sim}) from the generative model r_{syn} obtained in Sect. 7.1 to produce the contaminated map ($m_{\text{sim}} = s_{\text{sim}} + r_{\text{sim}}$). The Pearson correlation coefficient ρ of s_{sim} with the $N_{\text{H I}}$ map for $SNR = 3$ is 0.94, and is reduced to 0.88 after adding the contamination map r_{sim} . The upper panel of Fig. 6 shows the input dust map at $SNR = 3$, one random realization of the contamination, and the total contaminated simulated map. m_{sim} map is patchy owing to contamination.

7.3. Component separation algorithm validation

We apply the component separation algorithm described in Sect. 6.2 to the contaminated map to extract a statistical realization of the dust signal. By performing the component separation under different initial conditions, we obtain 25 recovered dust maps. The top panel of Fig. 6 shows one of the recovered dust maps (\tilde{s}_{sim}) and the residual map ($\tilde{r}_{\text{sim}} = m_{\text{sim}} - \tilde{s}_{\text{sim}}$). The value of ρ between s_{sim} and \tilde{s}_{sim} is found to be 0.97, showing a tight pixel-to-pixel correlation between the input and recovered dust maps. Visually, we can see that the small-scale features dominated by contamination are well separated from the large-scale dust emission. The lower panel of Fig. 6 shows s_{sim} , \tilde{s}_{sim} and their difference ($\delta_s = \tilde{s}_{\text{sim}} - s_{\text{sim}}$). The difference between the input and recovered dust (δ_s) has no visible large-scale features at the map level. The correlation coefficient $\rho = 0.91$ between \tilde{s}_{sim} and $N_{\text{H I}}$ is the same as that obtained between s_{sim} and $N_{\text{H I}}$. This shows that the component separation algorithm removes most of the contamination from the total map.

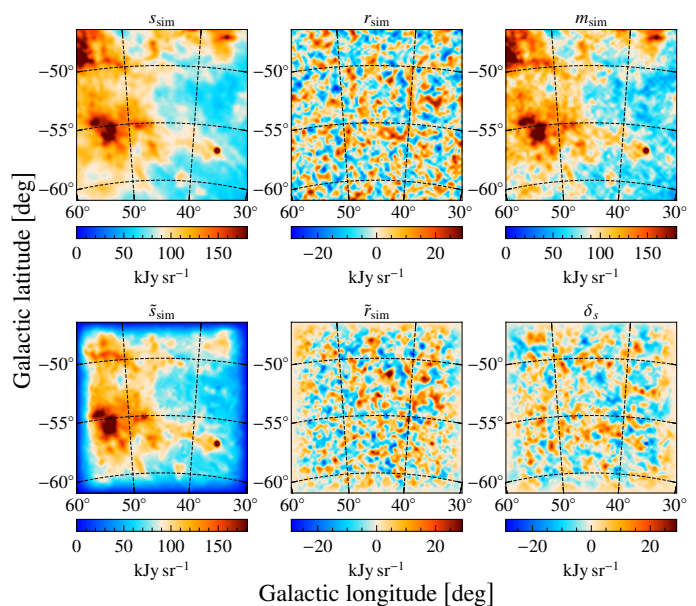


Fig. 6. Upper panel: input maps at $SNR = 3$ centered around the sky patch at $(l, b) = (45.0^\circ, -54.3^\circ)$. Columns from left to right show the input dust map (s_{sim}), the input contamination map (r_{sim}) and the total simulated map (m_{sim}). Lower panel: Columns from left to right shows the component separated dust map (\tilde{s}_{sim}), the residual map (\tilde{r}_{sim}), and the difference between input and recovered dust map (δ_s). The boundary pixels of the component separated maps (\tilde{s}_{sim} , \tilde{r}_{sim} , and δ_s) are apodised.

Next, we calculate the SC statistics (S_1 , S_2 , \bar{S}_3 , and \bar{S}_4) of these maps. The mean and standard deviation of S_1 and S_2 for five different j values and four different γ values, computed from 25 recovered dust maps, are shown in Fig. 7. Our component separation algorithm allows for the accurate recovery of these statistical properties of the dust map as a function of wavelet scales and orientations. The presence of contamination in m_{sim} leads to higher S_1 and S_2 at small scales (or low j values) compared to s_{sim} . The algorithm recovers almost all the scales of s_{sim} , apart from the smallest scales at $SNR = 3$. We show the remaining two SC statistics \bar{S}_3 and \bar{S}_4 in Appendix B. When we go to $SNR \geq 5$, the algorithm recovers S_1 and S_2 statistics for both large and small scales. Figure 8 shows the angle-averaged S_1 and S_2 statistics of r_{sim} and \tilde{r}_{sim} for different values of j . As the contamination maps are statistically isotropic, there is no preferred orientation where we expect to see more power. For r_{sim} ,

we compute the 1σ standard deviation from 300 r_{syn} maps. In the same plot, we also show the same angle-averaged S_1 and S_2 statistics of the δ_s map. The cross S_1 and S_2 statistics between r_{sim} and \tilde{r}_{sim} broadly follow the same statistics as r_{sim} . This means that the \tilde{r}_{sim} map retains the phase information of the input r_{sim} up to a certain percentage. Even though visually δ_s looks similar to r_{sim} , the amplitude of S_2 is much less than r_{sim} at small scales corresponding to low j values. Except for very large scales ($j = 4$), the power of δ_s is always less the power of \tilde{r}_{sim} . The 1σ deviation on the auto- and cross-statistics with the recovered maps are computed from the 25 realisations of \tilde{r} . Figure 9 shows the angle-averaged cross-statistics S_2 between \tilde{r}_{sim} and N_{HI} map. The errorbar on S_2 is computed from 25 realisations of the \tilde{r}_{sim} , starting from different initial conditions. For completeness, we compute the expected cross-statistics S_2 between r_{syn} and N_{HI} map. The mean value of the S_2 statistics computed from 300 r_{syn} maps is consistent with zero and 1σ errorbars capture patch-to-patch variations of the same statistics. Since we have added a single realisation of the contamination to

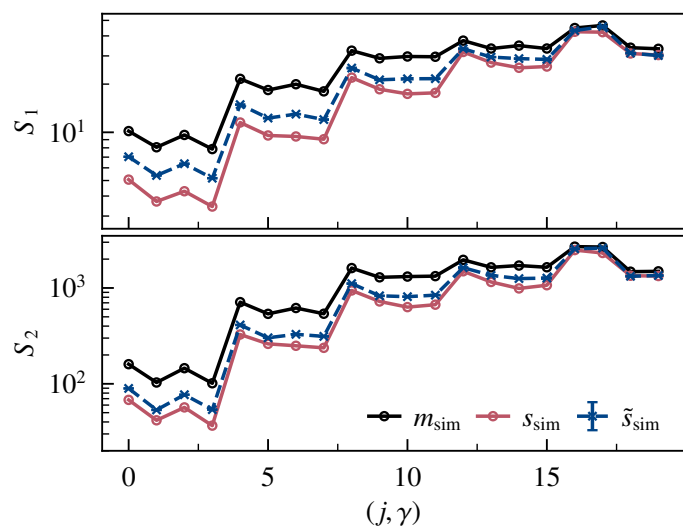


Fig. 7. Comparison of S_1 and S_2 statistics of m_{sim} (black circles), s_{sim} (red circles) and the \tilde{r}_{sim} (blue crosses with dashed line).

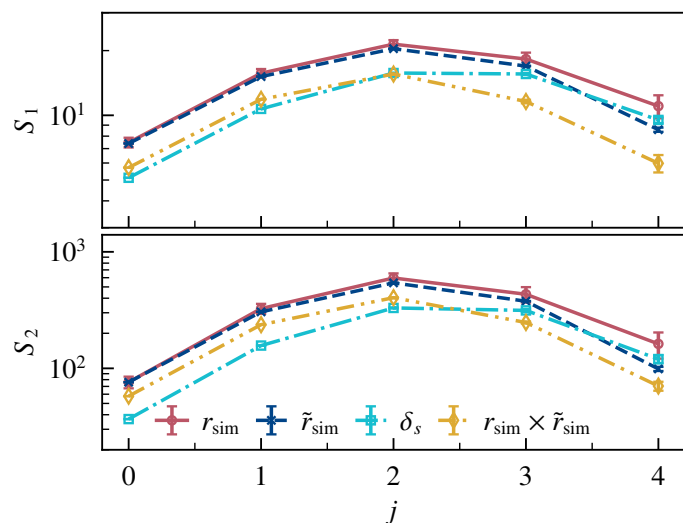


Fig. 8. Comparison of angle-averaged S_1 and S_2 statistics of r_{sim} (red circles), \tilde{r}_{sim} (blue crosses with dashed line) and the δ_s (cyan squares with dashed-dot line). The orange diamonds with dashed-dot-dot line show the cross coefficients between r_{sim} and \tilde{r}_{sim} .

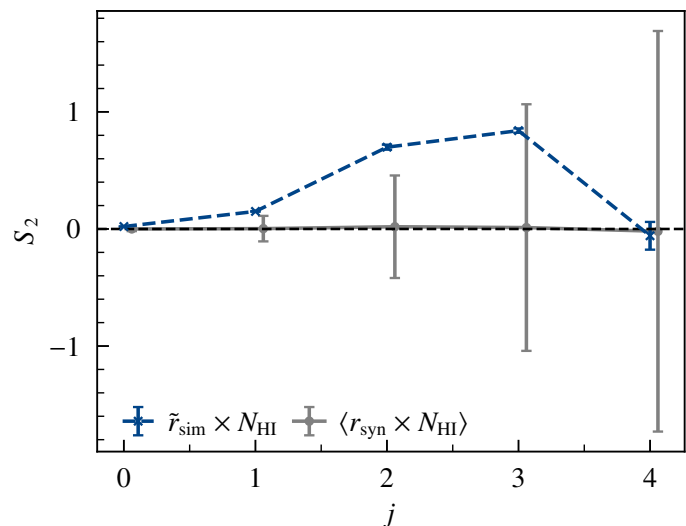


Fig. 9. Comparison of angle-averaged S_1 and S_2 cross-statistics between \tilde{r}_{sim} and N_{HI} map (blue crosses with dashed line), and r_{syn} and N_{HI} map averaged over 300 r_{syn} (gray circles). The cross-statistics of the recovered contamination map with N_{HI} are consistent within 1σ errorbars of the expected statistics. The gray circles are shifted in the x -axis.

the input dust map, the errorbar on $\tilde{r}_{\text{sim}} \times N_{\text{HI}}$ cross-statistics S_2 only includes the statistical noise due to the component separation algorithm.

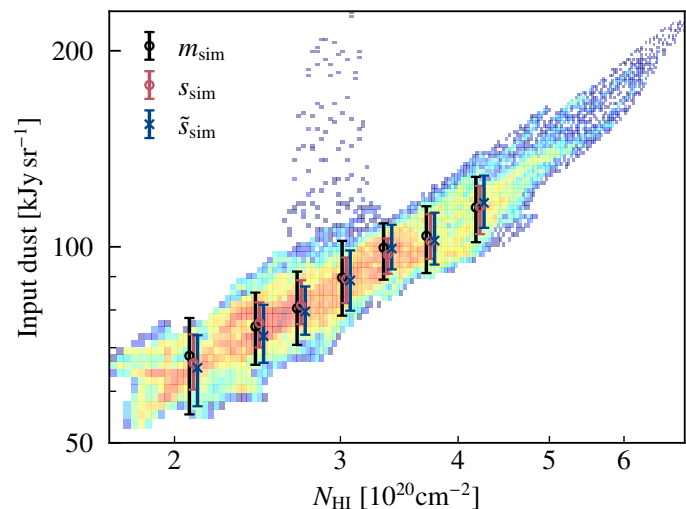


Fig. 10. 2D histogram showing the joint distribution of s_{sim} and N_{HI} . The black circles correspond to the median values and the upper and lower limits correspond to the 16 and 84 percentile of m_{sim} of the data in each ordered bin of N_{HI} . Similarly, the red circles are for s_{sim} and the blue crosses are for \tilde{r}_{sim} .

In Fig. 10, we plot 2D histogram highlighting the joint distribution of s_{sim} and N_{HI} . This shows that the s_{sim} has a significant amount of scatter with N_{HI} over the entire patch, and the correlation between them becomes non-linear above $N_{\text{HI}} > 4 \times 10^{20} \text{cm}^{-2}$. Next, we bin the data into 7 bins in order of increasing values of N_{HI} , and compute the median values of m_{sim} , s_{sim} and \tilde{r}_{sim} over each bin. The upper and lower limit of the errorbars at each bin correspond to the 16 and 84 percentile of the three quantities: m_{sim} , s_{sim} and \tilde{r}_{sim} . We see from this plot that the distributions are very similar for these different maps, although there appears to be a consistent reduction in the standard devia-

tion of the distribution at fixed N_{H_1} values from m_{sim} to \tilde{s}_{sim} . This effect is more pronounced at low N_{H_1} regions where the contamination is comparable to the dust signal. The reduction of the errorbars going from m_{sim} to \tilde{s}_{sim} is consistent with the expected outcome of removing contaminants.

Next, we vary the SNR of the dust signal with respect to contamination. For each SNR , we quantify the reliability of the component separation algorithm. For $SNR \geq 3$, we demonstrate that our component separation algorithm successfully and efficiently separates the dust signal from the contamination at the level of summary statistics. The algorithm only recovers the dust signal at large scales for low $SNRs$ ($SNR \approx 1$), leaving excess power at small scales in the recovered dust map. We apply the same procedure to other sky regions for different $SNRs$ and reach the same conclusions.

8. Application to *Planck* data

8.1. Component separated maps and its summary statistics

In this section, for brevity we will primarily focus on the component separation results on a sky patch of 222 deg^2 area centered at Galactic coordinates $(l, b) = (247.5^\circ, 66.4^\circ)$. We first subtract the CIB monopole term of 0.12 MJy sr^{-1} (Planck 2018 results. I. 2020) from the CMB-subtracted *Planck* data to focus only on the statistical separation of the dust emission and CIB contamination using the SC-based statistics. We refer to this map as m_d . The mean H I column density measured across the entire map is $\langle N_{\text{H}_1} \rangle = 2.3 \times 10^{20} \text{ cm}^{-2}$. The Pearson correlation coefficient ρ between the m_d and N_{H_1} maps is 0.84.

We apply the component separation algorithm to extract a statistical realization of the dust signal. We follow the same steps as described in Sect. 7. The upper panel of Fig. 11 shows the input map (m_d), recovered residual map (\tilde{r}) and dust map (\tilde{s}). The recovered dust map retains most of the large-scale features present in the *Planck* data, and filters out the small-scale fluctuations coming from the contamination. The mean dust emissivity over the entire sky patch is computed as the mean of the ratio of the recovered dust over N_{H_1} , defined as $\langle \epsilon \rangle = \langle \tilde{s}/N_{\text{H}_1} \rangle$. The mean value of the dust emissivity is $45 \text{ kJy sr}^{-1} (10^{20} \text{ cm}^{-2})$, which is consistent with the value obtained by Planck early results. XXIV. (2011); Planck intermediate results. XVII. (2014) and Adak et al. (2024).

Next, we present the statistics of the residual map (\tilde{r}). The top panel in Fig. 12, we show the joint distribution of \tilde{r} and the N_{H_1} map. The black data points are the median values and the error bars correspond to 1σ standard deviation in 7 bins ordered in increasing values of N_{H_1} . The median values are consistent with zero, showing no significant leakage of \tilde{s} into the residual map. The plot also confirms that our SC statistics based component separation algorithm works well for the $SNR \approx 8.4$ region. The standard deviation of $\sigma_{\tilde{r}}$ over the masked region is 8.1 kJy sr^{-1} , which is consistent with the expected value from 300 r_{syn} maps. In the middle panel of Fig. 12, we show the S_2 comparison of the \tilde{r} map in the *Planck* field and the expected distribution from 300 r_{syn} maps. The amplitudes of S_2 statistics match well at low j values, except for the very large scale ($j = 4$). The difference in S_2 statistics between \tilde{r} and 300 r_{syn} map is at the level of 2.3σ for $j = 4$. We also compare the CIB/LSS map (r_{LSS}) at $100 \mu\text{m}$ from Chiang (2023) at that field. We multiply the r_{LSS} map (in kJy sr^{-1} units) by a factor of 0.3 and compute the S_2 coefficient and find small-scales power are missing from the r_{LSS} map but the intermediate and large scales are consistent within the error bands from the synthetic maps. We correlate the \tilde{s} map with \tilde{r}

map and find a cross-correlation coefficient $\rho = -0.06$ between the two maps. We show the cross S_2 statistics of \tilde{s} and \tilde{r} in the lower panel of Fig. 12, to ensure that the recovered maps are statistically uncorrelated at the level of S_2 statistics. The 1σ deviations on the coefficients are computed from the cross S_2 statistics of \tilde{s} and the 300 r_{syn} maps. We also compute the cross statistics S_2 between \tilde{s} and r_{LSS} map for the same sky patch. The 1σ deviations on S_2 are computed from the cross statistics of \tilde{s} with 94 independent sky patches of size $14.9^\circ \times 14.9^\circ$ of the Chiang (2023) CIB/LSS map. All the scales are consistent with the zero within 1σ errorbar, except for $j = 2$ scale where the deviation is at the level of 3.2σ . We find the cross-correlation coefficient of the \tilde{s} map with r_{LSS} map to be $\rho = 0.03$.

Appendix C presents the component separation results for the same *Planck* field as used for the validation of the component separation algorithm in Sect. 7.

8.2. Separation in H I and H₂ emission

To understand the morphology of the recovered dust emission, we decompose it into two components: dust associated with N_{H_1} (\tilde{s}_{H_1}) and dust associated with N_{H_2} (\tilde{s}_{H_2})

$$\tilde{s} = \tilde{s}_{\text{H}_1} + \tilde{s}_{\text{H}_2}, \quad (18)$$

where $\tilde{s}_{\text{H}_1} = \epsilon_{\text{H}_1,353} N_{\text{H}_1}$ and $\epsilon_{\text{H}_1,353}$ is the dust emissivity of the H I-correlated dust emission at 353 GHz. In our case, $\epsilon_{\text{H}_1,353}$ is a constant value over the selected sky patch. We estimate the mean $\langle \epsilon_{\text{H}_1,353} \rangle$ from the square patches, defined in Sect. 4, at high Galactic latitudes. We apply the final iterative mask (discussed in Sect. 3) to the high-latitude square patches to select only the low N_{H_1} pixels where the dust-H I correlation holds. We also avoid square patches where more than 30% pixels are masked. Finally, we are left with 40 such high-latitude square patches where sufficient number of valid pixels are available for the correlation analysis. Using a simple linear regression with the N_{H_1} map, we find a value of emissivity per square patch. While performing linear regression, we take into account the standard deviation of the contamination as an errorbar per pixel. By analysing 40 sky patches, we obtain the mean and standard deviation of the dust emissivity as $\langle \epsilon_{\text{H}_1,353} \rangle = 38 \pm 6 \text{ kJy sr}^{-1} (10^{20} \text{ cm}^{-2})$. We produce 100 realizations of the $\tilde{s}_{N_{\text{H}_1}}$ maps by varying $\epsilon_{\text{H}_1,353}$ within the mean and standard deviation of this estimate. The lower panel of Fig. 11 shows the decomposition of \tilde{s} in terms of the \tilde{s}_{H_1} (left panel) and \tilde{s}_{H_2} (middle panel) using the value of $\langle \epsilon_{\text{H}_1,353} \rangle$. Visually, we can see that \tilde{s}_{H_2} map is clumpy whereas the \tilde{s}_{H_1} map is more diffuse.

We compute the SC statistics of the \tilde{s}_{H_1} and \tilde{s}_{H_2} maps to characterize their morphological differences. We use S_1 and S_2 statistics, and the S_1^2/S_2 ratio to measure sparsity (Lei et al. 2025). Figure 13 shows the variation of S_1 , S_2 and S_1^2/S_2 as a function of j and γ . The errorbars on the SC statistics of the $\tilde{s}_{N_{\text{H}_2}}$ map are computed from the 100 realizations of $\tilde{s}_{N_{\text{H}_2}}$ maps. The first order coefficient S_1 and wavelet power spectrum S_2 show that the \tilde{s}_{H_1} map has more power at large angular scales and across all orientations compared to that of the $\tilde{s}_{N_{\text{H}_2}}$ map. The lower values of the ratio S_1^2/S_2 for \tilde{s}_{H_2} compared to the \tilde{s}_{H_1} map shows that \tilde{s}_{H_2} map is significantly sparser than \tilde{s}_{H_1} , as the ratio decreases with an increase in the sparsity of the field. This is consistent with Fig. 11 where the localised high column density structures are only present in the \tilde{s}_{H_2} map.

Next, we compute the power spectrum of \tilde{s} and compare with the power spectrum of N_{H_1} . Because of the limited sky coverage of the sky patch, the largest scale we obtain is $\ell \approx 25$. We fit

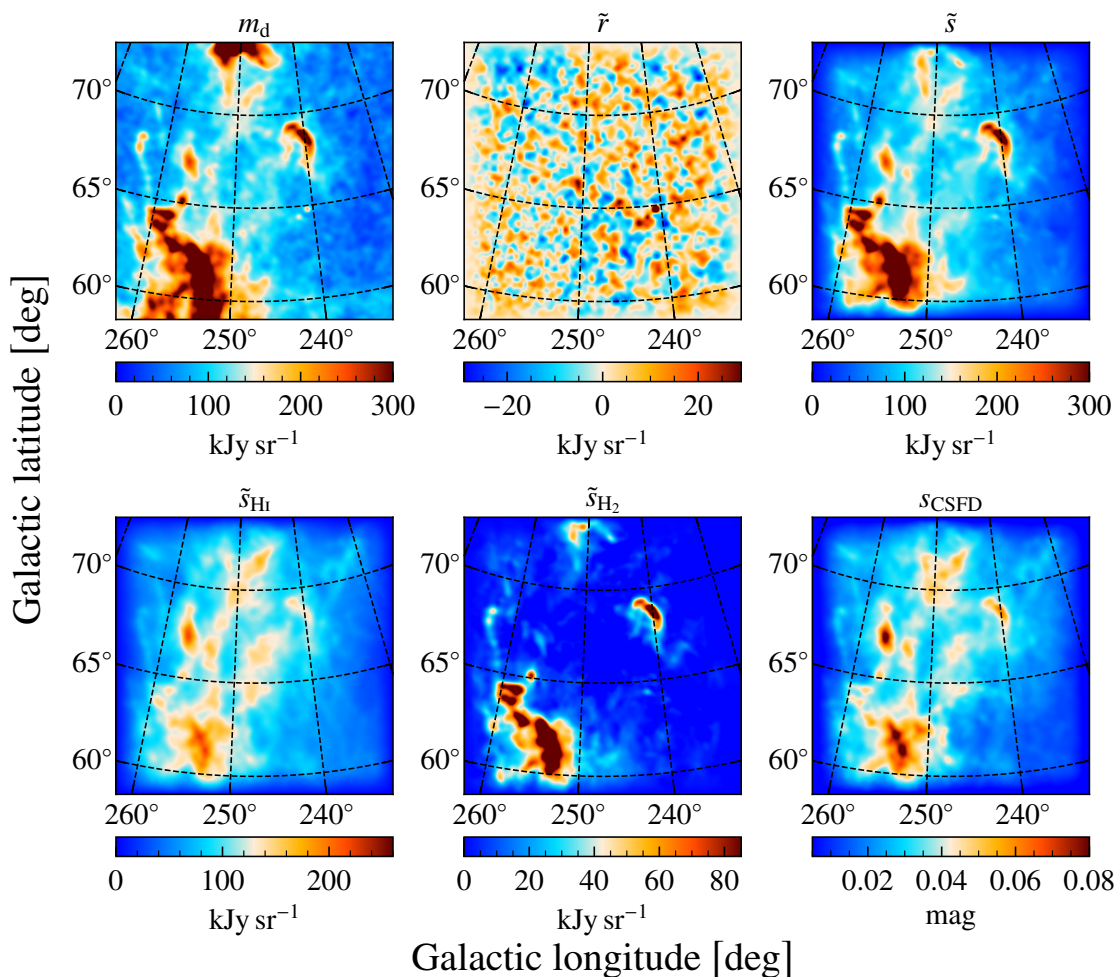


Fig. 11. *Upper panel:* The *Planck* 353 GHz map (CMB and CIB monopole subtracted; left) and the recovered residual map (middle) and dust map (right) after component separation at the same sky region as in Fig. 6. *Lower panel:* The decomposed \tilde{s}_{H_1} (left) and \tilde{s}_{H_2} maps (middle). The CSFD reddening map at 100 μm in mag at the same sky region is shown in the right panel.

them with a power-law model, $C_\ell \propto (\ell/75)^\alpha$, in the multipole range $25 \leq \ell \leq 625$ and find the best-fit value of the exponents as $\alpha_{\tilde{s}} = -2.50 \pm 0.07$ and $\alpha_{\text{H}_1} = -2.92 \pm 0.10$, respectively. The difference in the slope of \tilde{s} and N_{H_1} spectrum, $\Delta\alpha = \alpha_{\tilde{s}} - \alpha_{\text{H}_1} \approx 0.4$, also hints toward the presence of significant amount of dust emission associated with gas in the form of H_2 (Desert et al. 1988; Reach et al. 1998).

8.3. Comparison of our dust map with CSFD extinction map

In this section, we compare the recovered *Planck* dust map at 353 GHz with the CSFD map at 100 μm over the same sky patch as discussed in Sect. 8.1. The right column of Fig. 11 shows the map-level comparison between \tilde{s} (expressed in units of kJy sr^{-1}) and s_{CSFD} (expressed in units of mag). Our first observation is that there are more localised structures present in the *Planck* dust map than in the CSFD map. This finding is supported by the power spectrum comparison between the two maps. We compute the power spectrum of \tilde{s} and s_{CSFD} over the apodised mask and fit it with a power-law model within the multipole range $\ell \in [25, 625]$. The power spectrum exponent for the *Planck* dust map is $\alpha_{\tilde{s}} = -2.50 \pm 0.07$ and that for the CSFD map is $\alpha_{s_{\text{CSFD}}} = -2.65 \pm 0.09$.

Next, we compute the non-linear dependence of \tilde{s} and s_{CSFD} on N_{H_1} map by fitting a power-law model, $(\tilde{s}, s_{\text{CSFD}}) \propto \langle N_{\text{H}_1} \rangle^p$. The power-law exponent p is expected to be close to 1 in case of tight correlation between dust and atomic gas holds true. For each of the two dust maps, we group the pixel values into 7 bins in ascending order of N_{H_1} and compute the median values within each N_{H_1} bin, as well as the 16 and 84 percentiles, which we use as error bars. We fit the median values \tilde{s} and s_{CSFD} with the mean N_{H_1} (taking into account the error bars) and find that the value of the exponent p is 1.05 for the *Planck* map and 0.85 for the CSFD map. This result shows that the slope of the power-law differs significantly between the *Planck* and CSFD maps. Furthermore, the data scatter in the N_{H_1} correlation is greater for \tilde{s} than for the s_{CSFD} map.

The morphological differences seen between the recovered *Planck* dust map and CSFD map can be explained by different spectral energy distribution (SED) of H_1 -correlated dust emission and H_2 -correlated dust emission. If both the SEDs follow the modified blackbody spectrum (MBB), then the ratio of the emissivities of the H_1 and H_2 -correlated dust components at 353 GHz can be written as

$$\frac{\epsilon_{\text{H}_1, 353}}{\epsilon_{\text{H}_2, 353}} = \left(\frac{353}{\nu_0} \right)^{(\beta_{\text{H}_1} - \beta_{\text{H}_2})} \frac{B_{353}(T_{\text{H}_1})}{B_{\nu_0}(T_{\text{H}_1})} \frac{B_{\nu_0}(T_{\text{H}_2})}{B_{353}(T_{\text{H}_2})}, \quad (19)$$

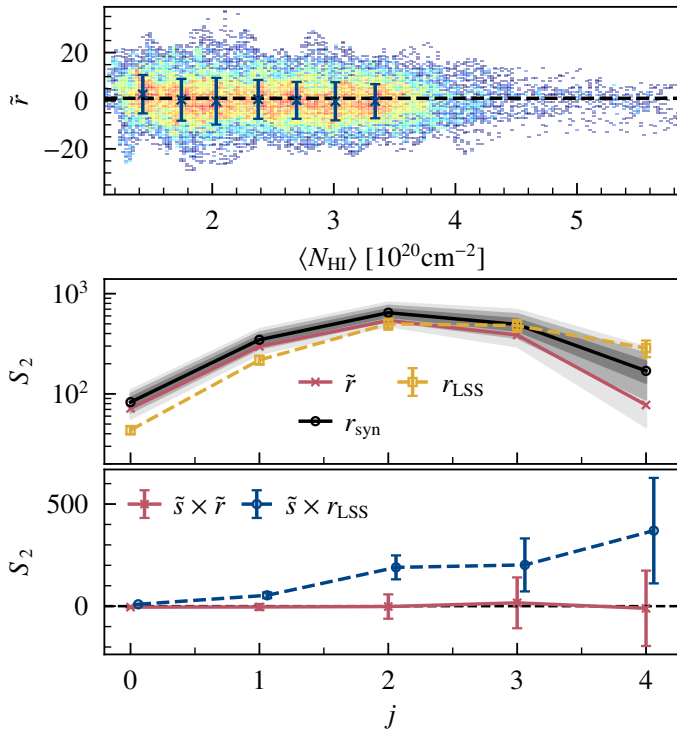


Fig. 12. *Upper panel:* Correlation plot of \tilde{r} with N_{HI} map. The blue data points and the errorbars show the zero median and standard deviation of \tilde{r} in the ordered bins of N_{HI} . The standard deviations are consistent in all the N_{HI} bins. *Middle panel:* Comparison of angle-averaged S_2 statistics of \tilde{r} (red cross), r_{LSS} (orange square dashed line) and the ensemble average of 300 r_{syn} maps (black circles) along with 1σ , 2σ and 3σ error-bands. *Lower panel:* The red crosses with solid line show cross S_2 coefficients between $\tilde{\delta}$ and \tilde{r} and blue circles with dashed line show the cross S_2 coefficients between $\tilde{\delta}$ and r_{LSS} . The blue circles are slightly shifted in the x -axis.

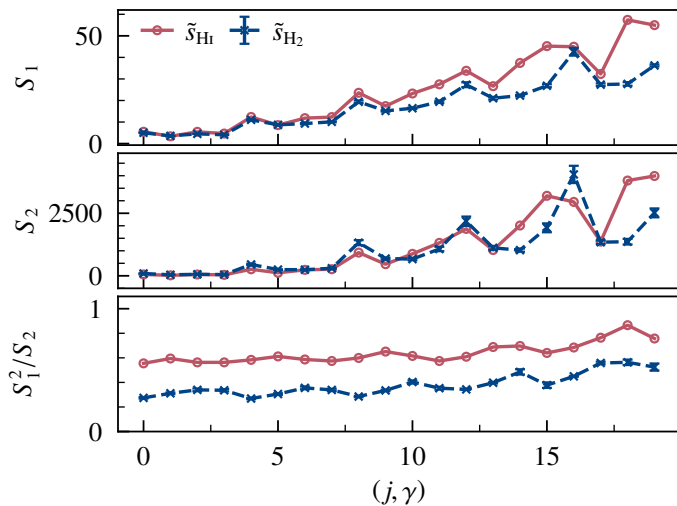


Fig. 13. S_1 , S_2 , S_1^2/S_2 for the $\tilde{\delta}_{\text{H1}}$ map (red circles) and the $\tilde{\delta}_{\text{H2}}$ maps (blue crosses with dashed line). The standard deviation is obtained from 100 realisations of $\tilde{\delta}_{\text{H2}}$ maps (blue crosses with dashed line).

where $\nu_0 = 100\mu\text{m}$ is the reference frequency and $B_{353}(T)$ is the Planck blackbody function at 353 GHz. Here $(T_{\text{H1}}, \beta_{\text{H1}})$ and $(T_{\text{H2}}, \beta_{\text{H2}})$ are temperatures and spectral indices of the H1 and H2-associated dust emission, respectively. We assume that the ratio $\epsilon_{\text{H1},100\mu\text{m}}/\epsilon_{\text{H2},100\mu\text{m}} = 1$. If we neglect attenuation of the interstellar radiation field by dust within the diffuse interstel-

lar medium, the integral of MBB spectrum or the dust radiance (given by Equation 10 in [Planck 2013 results. XI. \(2014\)](#)) does not vary from H1 to the H2 gas. Under these two assumptions, we can write a constraint relation between the SED parameters of H1 and H2-associated dust emission as

$$\frac{T_{\text{H2}}^{(\beta_{\text{H2}}+4)} \nu_0^{-\beta_{\text{H2}}} \Gamma(\beta_{\text{H2}}+4) \zeta(\beta_{\text{H2}}+4)}{T_{\text{H1}}^{(\beta_{\text{H1}}+4)} \nu_0^{-\beta_{\text{H1}}} \Gamma(\beta_{\text{H1}}+4) \zeta(\beta_{\text{H1}}+4)} = 1. \quad (20)$$

We adopt $T_{\text{H1}} = 20$ K and $\beta_{\text{H1}} = 1.65$ from [Planck intermediate results. XVII. \(2014\)](#), computed from the MBB fit to the dust emissivities at the far-infrared frequencies 353, 545 and 857 GHz and COBE-DIRBE $100\mu\text{m}$, for the H1-correlated dust emission. The change in β_{H2} will follow from that of T_{H2} and thus the change in relative grain emissivity at 353 GHz. We fit s_{CSFD} map with two-templates ($\tilde{\delta}_{\text{H1}}$ and $\tilde{\delta}_{\text{H2}}$) and a constant offset (O) over the valid pixels within the binary mask. We model the s_{CSFD} map as

$$\begin{aligned} s_{\text{CSFD}} &= a_{\text{H1}} \tilde{\delta}_{\text{H1}} + a_{\text{H2}} \tilde{\delta}_{\text{H2}} + O, \\ &= a_{\text{H1}} \epsilon_{\text{H1},353} \left(N_{\text{H1}} + \frac{a_{\text{H2}} \tilde{\delta}_{\text{H2}}}{a_{\text{H1}} \epsilon_{\text{H1},353}} \right) + O, \\ &= \epsilon_{\text{H1},100\mu\text{m}} (N_{\text{H1}} + 2N_{\text{H2}}) + O. \end{aligned} \quad (21)$$

The best-fit values of a_{H1} is $0.32 \pm 0.06 \text{ mag}(\text{MJy sr}^{-1})^{-1}$ and a_{H2} is $0.0321 \pm 0.0003 \text{ mag}(\text{MJy sr}^{-1})^{-1}$. By defining $2N_{\text{H2}}$ map as $a_{\text{H2}} \tilde{\delta}_{\text{H2}} / (a_{\text{H1}} \epsilon_{\text{H1},353})$, we enforce the emissivities of both H1 and H2-correlated dust emission to be the same at $100\mu\text{m}$. Writing, $\tilde{\delta}_{\text{H2}} = \epsilon_{\text{H2},353} (2N_{\text{H2}})$, the ratio between the H1-correlated dust emission and H2-correlated dust emission at 353 GHz is obtained as $\epsilon_{\text{H1},353} / \epsilon_{\text{H2},353} = 0.11 \pm 0.01$. The observed ratio can be achieved by assuming that the H2-correlated dust emission has a temperature of $T_{\text{H2}} = 18.5$ K and spectral index $\beta_{\text{H2}} = 0.81$, which is different from the SED parameters of the H1-correlated emission. Recently, [Sullivan et al. \(2026\)](#) reported compelling evidence for two distinct dust emission components — referred to as “hot dust” and “cold dust” in the *Planck* data, lending further support to our results.

9. Summary and discussion

In this work, we statistically separate the dust signal from the CIB contamination at 353 GHz using the SC statistics. We use N_{HI} map as an external tracer to minimize the leakage of the contamination into the recovered dust signal map. To do so, the component separation algorithm relies on a set of loss functions so that the recovered dust map retains the spatial correlation with the N_{HI} map as present in the input data and the contamination is statistically uncorrelated with the N_{HI} map. A brief summary and the main results of the analysis are as follows:

- We first analysed 25 square patches of the contamination map obtained at low N_{HI} regions using the template-fit approach, taking into account the pixel-dependent dust emissivity and a global offset. The standard deviation of the contamination map and its angular power spectrum obtained from 25 square patches are statistically consistent with each other. The three scalar MFs derived from these patches closely follow the expected values from a Gaussian distribution of CIB following the [Lenz et al. \(2019\)](#) best-fit CIB model plus instrumental noise contribution from FFP10 simulations.

- We synthesize 300 realisations of the contamination map using the Scattering Transform statistics based on the maximum entropy generative model. By construction, the 300 synthesised contamination maps have the same statistical properties (summary statistics, angular power spectrum, and the three scalar MFs) as the 25 contamination maps obtained from the template-fit approach at low $N_{\text{H}1}$ regions.
- We validate our algorithm on a simulated 2D test patch centered at Galactic coordinates $(l, b) = (45.0^\circ, -54.3^\circ)$. We use the interstellar dust reddening map from [Chiang \(2023\)](#) as a proxy of the dust emission and scale its amplitude to different $SNRs$ with respect to the contamination map. We add a synthesised realization of the contamination to the simulated dust map. We compute the SC statistics of the input and recovered dust maps and the cross SC statistics of the residual map with $N_{\text{H}1}$ to conclude that the component separation algorithm works fairly well for $SNR \geq 3$ case. There is no significant leakage of the dust emission into the contamination map. We have verified that the recovered contamination map is uncorrelated with the $N_{\text{H}1}$ map in the pixel space and in terms of S_2 statistics. We test our component separation algorithm on other sky patches and reach to the same conclusions.
- We successfully applied the component separation algorithm to a same test patch in the *Planck* data ($SNR \approx 8.4$) and separate the dust signal (\tilde{s}) from the contamination.
- We decompose the component-separated *Planck* dust map at 353 GHz into a diffuse H I -correlated dust emission ($\tilde{s}_{\text{H}1}$) and a clumpy H_2 -correlated dust emission ($\tilde{s}_{\text{H}2}$). The presence of the significant amount of dust associated with H_2 gas in the \tilde{s} can explain the difference in the power-law slopes of the \tilde{s} and $N_{\text{H}1}$ angular power spectra. We use the SC statistics to understand the morphological difference between the two component. The $\tilde{s}_{\text{H}2}$ map is found to be more sparse, but less filamentary in nature as compared to $\tilde{s}_{\text{H}1}$ map.
- We also compare the component-separated dust map with the CSFD map at $100 \mu\text{m}$ for this region. The CSFD map has tighter correlated with the $N_{\text{H}1}$ map as compared to the \tilde{s} map. The maps as well as the difference in power spectra exponents show that the \tilde{s} has more localised structures in it as compared to the CSFD map.

This paper opens the way to produce dust reddening map using the *Planck* data. The decomposition of the dust map (free from CIB contamination) into $N_{\text{H}1}$ and $N_{\text{H}2}$ components helps us to investigate the formation of H_2 gas within the diffuse ISM. In the future paper, we will analyse all the available *Planck* high-frequency data ($\nu \geq 217$ GHz) to model the component-separated dust emission in terms of modified black-body spectrum. The next step is to expand the dust-CIB separation problem to encompass the full sky using the Foscat software package. Producing clean dust maps, devoid of any CIB contamination, across all HFI frequencies is crucial for determining the spectral energy distribution of dust emission and for validating the dust- H I correlation in regions of low H I column density regions.

Acknowledgements. We thank Constant Auclair for the useful discussion and help during the start of the project. Some of the results in this paper have been derived using the HEALPix package. We acknowledge use of the *Planck* Legacy Archive. *Planck* is an ESA science mission with instruments and contributions directly funded by ESA Member States, NASA, and Canada. The Parkes Radio Telescope is part of the Australia Telescope National Facility which is funded by the Australian Government for operation as a National Facility managed by CSIRO. The EBHIS data are based on observations performed with the 100-m telescope of the MPIfR at Effelsberg. EBHIS was funded by the Deutsche Forschungsgemeinschaft (DFG) under the grants KE757/7-1 to 7-3. The computations in this paper were run on the GPU cluster at NISER supported by the

Department of Atomic Energy of the Government of India. S. S. is supported by the National Postdoctoral Fellowship of the Science and Engineering Research Board (SERB), ANRF, Government of India (File No.: PDF/2023/000594). This work received government funding managed by the French National Research Agency under France 2030, reference numbers “ANR-23-IACL-0008” and “ANR-25-CE46-6634”.

References

- Adak, D., Shaikh, S., Sinha, S., et al. 2024, *Monthly Notices of the Royal Astronomical Society*, 531, 4876
- Allys, E., Marchand, T., Cardoso, J.-F., et al. 2020, *Phys. Rev. D*, 102, 103506
- Allys, E., Levrier, F., Zhang, S., et al. 2019, *A&A*, 629, A115
- Alonso, D., Sanchez, J., Slosar, A., & Collaboration, L. D. E. S. 2019, *Monthly Notices of the Royal Astronomical Society*, 484, 4127
- Andén, J. & Mallat, S. 2014, *IEEE Transactions on Signal Processing*, 62, 4114
- Auclair, Constant, Allys, Erwan, Boulanger, François, et al. 2024, *A&A*, 681, A1
- Béthermin, M., Dole, H., Beelen, A., & Aussel, H. 2010, *A&A*, 512, A78
- Blancard, B. R.-S., Allys, E., Auclair, C., et al. 2023, *The Astrophysical Journal*, 943, 9
- Boelens, A. M. P. & Tchepeli, H. A. 2021, *SoftwareX*, 16, 100823
- Boulanger, F., Abergel, A., Bernard, J. P., et al. 1996, *A&A*, 312, 256
- Boulanger, F. & Perault, M. 1988, *ApJ*, 330, 964
- Bruna, J. & Mallat, S. 2013, *IEEE Transactions on Pattern Analysis and Machine Intelligence*, 35, 1872
- Bruna, J. & Mallat, S. 2018, *Jour. of Math. Stat. and Learning*, 1, 257
- Campeti, P., Delouis, J. M., Pagano, L., et al. 2025, *A&A*, 700
- Cheng, S. & Ménard, B. 2021, arXiv e-prints, arXiv:2112.01288
- Cheng, S. & Ménard, B. 2021, *Monthly Notices of the Royal Astronomical Society*, 507, 1012
- Cheng, S., Morel, R., Allys, E., Ménard, B., & Mallat, S. 2024, *PNAS Nexus*, 3, pgae103
- Cheng, S., Ting, Y.-S., Ménard, B., & Bruna, J. 2020, *Monthly Notices of the Royal Astronomical Society*, 499, 5902
- Chiang, Y.-K. 2023, *The Astrophysical Journal*, 958, 118
- Chiang, Y.-K. & Ménard, B. 2019, *The Astrophysical Journal*, 870, 120
- Delouis, J.-M., Allys, E., Gauvrit, E., & Boulanger, F. 2022, *A&A*, 668, A122
- Desert, F. X., Bazell, D., & Boulanger, F. 1988, *ApJ*, 334, 815
- Dickey, J. M. & Lockman, F. J. 1990, *ARA&A*, 28, 215
- Draine, B. T. 2011, *Physics of the Interstellar and Intergalactic Medium*
- Eickenberg, M., Allys, E., Moradinezhad Dizgah, A., et al. 2022, arXiv e-prints, arXiv:2204.07646
- Górski, K. M., Hivon, E., Banday, A. J., et al. 2005, *ApJ*, 622, 759
- Greig, B., Ting, Y.-S., & Kurov, A. A. 2022, *Monthly Notices of the Royal Astronomical Society*, 513, 1719
- Hauser, M. G. & Dwek, E. 2001, *Annual Review of Astronomy and Astrophysics*, 39, 249
- Hayakawa, T. & Fukui, Y. 2024, *Monthly Notices of the Royal Astronomical Society*, 529, 1
- Hivon, E., Górski, K. M., Netterfield, C. B., et al. 2002, *ApJ*, 567, 2
- Hothi, I., Allys, E., Semelin, B., & Meriot, R. 2026, *A&A*, 706, A15
- Hothi, Ian, Allys, Erwan, Semelin, Benoît, & Boulanger, François. 2024, *A&A*, 686, A212
- Ichiki, K. 2014, *Progress of Theoretical and Experimental Physics*, 2014, 06B109
- Jeffrey, N., Boulanger, F., Wandelt, B. D., et al. 2021, *Monthly Notices of the Royal Astronomical Society: Letters*, 510, L1
- Kalberla, P. M. W., McClure-Griffiths, N. M., Pisano, D. J., et al. 2010, *A&A*, 521, A17
- Lagache, G., Puget, J.-L., & Dole, H. 2005, *Ann. Rev. Astron. Astrophys.*, 43, 727
- Larsen, P., Challinor, A., Sherwin, B. D., & Mak, D. 2016, *Phys. Rev. Lett.*, 117, 151102
- Lei, M. & Clark, S. E. 2023, *The Astrophysical Journal*, 947, 74
- Lei, M., Clark, S. E., Morel, R., et al. 2025, *The Astrophysical Journal*, 993, 4
- Lenz, D., Doré, O., & Lagache, G. 2019, *ApJ*, 883, 75
- Lenz, D., Flöer, L., & Kerp, J. 2016, *A&A*, 586, A121
- Mak, D. S. Y., Challinor, A., Efstathiou, G., & Lagache, G. 2017, *MNRAS*, 466, 286
- Maniyar, A. S., Béthermin, M., & Lagache, G. 2018, *A&A*, 614, A39
- Mantz, H., Jacobs, K., & Mecke, K. 2008, *Journal of Statistical Mechanics: Theory and Experiment*, 2008, P12015
- McCarthy, F. 2024, arXiv e-prints, arXiv:2405.13470
- McClure-Griffiths, N. M., Pisano, D. J., Calabretta, M. R., et al. 2009, *ApJS*, 181, 398
- Mouset, L., Allys, E., Price, M. A., et al. 2024, *A&A*, 691
- Planck* 2013 results. IX. 2014, *A&A*, 571, A9

Planck 2013 results. VIII. 2014, A&A, 571, A8
 Planck 2013 results. XI. 2014, A&A, 571, A11
 Planck 2013 results. XXX. 2014, A&A, 571, A30
 Planck 2015 results - XII. 2016, A&A, 594, A12
 Planck 2018 results. I. . 2020, A&A, 641, A1
 Planck 2018 results. III. 2020, A&A, 641, A3
 Planck 2018 results. IV. 2020, A&A, 641, A4
 Planck early results. XXIV. 2011, A&A, 536, A24
 Planck intermediate results. XLVIII. 2016, A&A, 596, A109
 Planck intermediate results. XVII. 2014, A&A, 566, A55
 Puget, J. L., Abergel, A., Bernard, J. P., et al. 1996, A&A, 308, L5
 Reach, W. T., Wall, W. F., & Odegard, N. 1998, ApJ, 507, 507
 Regaldo-Saint Blancard, B., Levrier, F., Allys, E., Bellomi, E., & Boulanger, F. 2020, A&A, 642, A217
 Regaldo-Saint Blancard, Bruno, Allys, Erwan, Boulanger, François, Levrier, François, & Jeffrey, Niall. 2021, A&A, 649, L18
 Richard, P., Allys, E., Levrier, F., Gusdorf, A., & Auclair, C. 2025, A&A, 696
 Robitaille, T., Deil, C., & Ginsburg, A. 2020, reproject: Python-based astronomical image reprojection, Astrophysics Source Code Library, record ascl:2011.023
 Saydjari, A. K., Portillo, S. K. N., Slepian, Z., et al. 2021, The Astrophysical Journal, 910, 122
 Schlegel, D. J., Finkbeiner, D. P., & Davis, M. 1998, ApJ, 500, 525
 Sullivan, R. M., Gjerløw, E., Galloway, M., et al. 2026, arXiv e-prints, arXiv:2601.10640
 Tsouros, A., Russier, E., Allys, E., et al. 2026, arXiv e-prints, arXiv:2602.04528
 Valogiannis, G. & Dvorkin, C. 2022, Phys. Rev. D, 105, 103534
 Viero, M. P., Reichardt, C. L., Benson, B. A., et al. 2019, The Astrophysical Journal, 881, 96
 Virtanen, P., Gommers, R., Oliphant, T. E., et al. 2020, Nature Methods, 17, 261
 Wakker, B. P. & Boulanger, F. 1986, A&A, 170, 84
 Winkel, B., Kerp, J., Flöer, L., et al. 2016, A&A, 585, A41

Appendix A: Masks

The binary and apodised masks used in this work are shown in Fig. A.1.

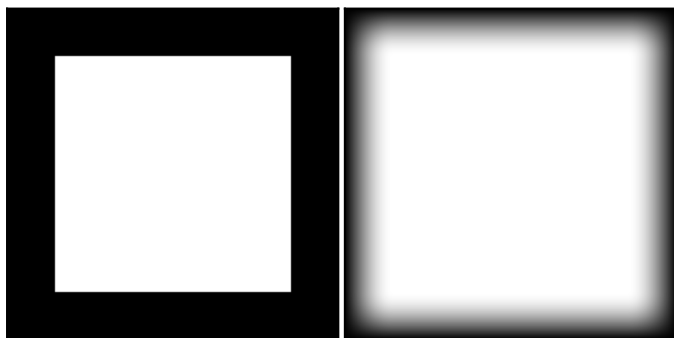


Fig. A.1. The binary mask (*left panel*) with inner 180×180 pixels and the 256×256 pixels apodised mask (*right panel*) used in our analysis.

Appendix B: Results for simulations

In Fig. B.1, we show the normalised SC statistics \bar{S}_3 and \bar{S}_4 for m_{sim} , s_{sim} and \tilde{s}_{sim} in lexicographic order. The algorithm preserves the correlations between the different wavelet scales present in s_{sim} .

Appendix C: Component separation results for the same *Planck* field as used in algorithm validation

For completeness, we show the results of the component separation algorithm for the *Planck* data region used to validate the component separation algorithm in Sect. 7. Assuming the mean standard deviation of contamination map of $\sigma_{r_{\text{syn}}} = 9.0 \text{ kJy sr}^{-1}$,

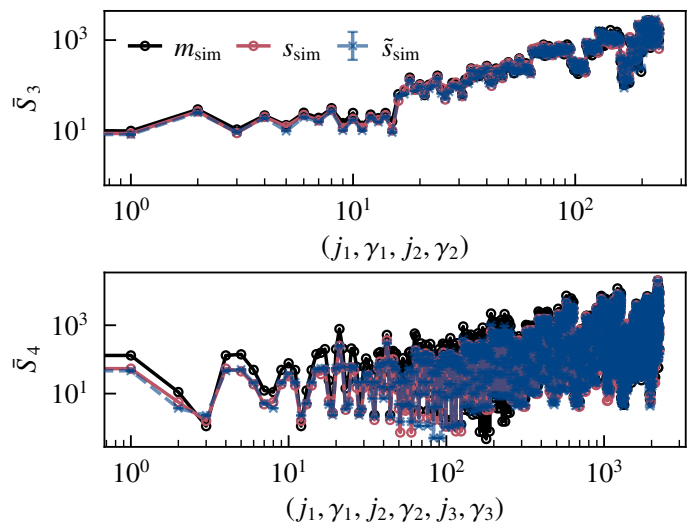


Fig. B.1. Comparison of \bar{S}_3 and \bar{S}_4 statistics between m_{sim} , s_{sim} and \tilde{s}_{sim} .

this specific sky patch in the *Planck* data has an $SNR \approx 5$. The first column of Fig. C.1 shows the *Planck* data (m_d), second column shows the recovered dust map (\tilde{s}), and third column shows (\tilde{r}) highlighting the difference between the *Planck* data and the recovered dust map. The standard deviation of \tilde{r} computed over the binary mask is 8.3 kJy sr^{-1} , consistent with the expected standard deviation of the $300 r_{\text{syn}}$ that are used as an input to the component separation algorithm.

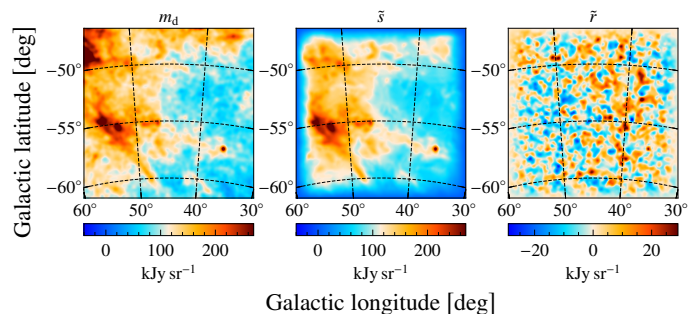


Fig. C.1. *Planck* data at 353 GHz (*left panel*), the recovered dust signal (*middle panel*) and residual (*right panel*) for the same sky region as used in Sect. 7.

The bright infrared point source centered at Galactic coordinates $(l, b) = (45.0^\circ, -54.3^\circ)$ is mostly present in the recovered dust map and a small fraction of it leaks into the residual map. We have applied a 1° cut around the point source to exclude it from the further analysis of the summary statistics and the power spectrum. Figure C.2 shows the S_1 and S_2 coefficients for m_d , \tilde{s} and \tilde{r} for the four different orientations of the wavelet. The m_d map at large scales (or high j values) is signal dominated. The contamination map, which is statistically isotropic, has roughly the same power in all four orientations.

Figure C.3 shows the power spectra of \tilde{s} and N_{HI} data for the same region. We apply 1° cut around the bright infrared point source to avoid any bias in the computation of the dust angular power spectrum. We fit the dust spectrum with the power-law model within the same multipole range as in Sect. 2.1. The straight lines in Fig. C.3 show the best-fit power-law models for the auto-power spectrum of \tilde{s} , cross-power spectrum of \tilde{s} with H I map, and auto-power spectrum of the H I map. The best-fit exponents are $\alpha_{\tilde{s}} = -2.52 \pm 0.11$, $\alpha_{\times} = -2.93 \pm 0.16$ and

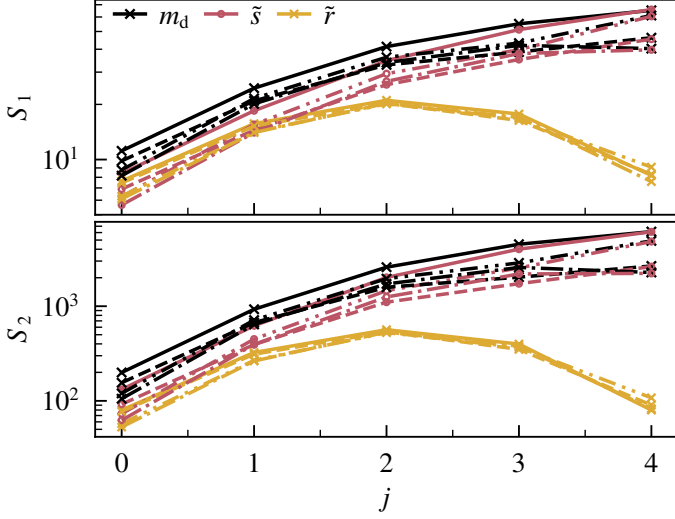


Fig. C.2. The S_1 and S_2 coefficients of the m_d , \tilde{s} and \tilde{r} maps. The four line types show the four different orientations.

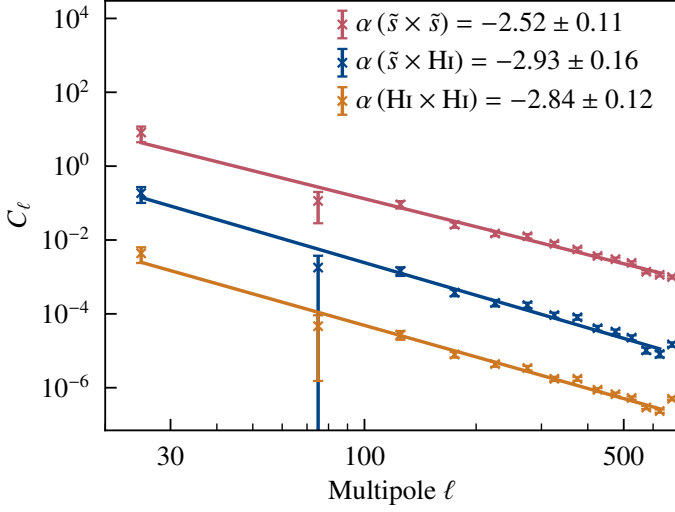


Fig. C.3. The red cross and line show the auto spectrum C_ℓ with ℓ of \tilde{s} along with the best-fit power-law model, respectively in the unit $\text{kJy}^2 \text{sr}^{-1}$. The blue cross shows the cross power spectrum of \tilde{s} and the H I data along with the best-fit power-law model in $\text{kJy sr}^{-1} (10^{20} \text{cm}^{-2})$ unit. The orange shows the auto spectrum of the total H I data with the best-fit model in $(10^{20} \text{cm}^{-2})^2$ unit.

$\alpha_{\text{H I}} = -2.84 \pm 0.12$, respectively. In this case, the difference in the slopes of \tilde{s} and $N_{\text{H I}}$ spectra, $\Delta\alpha = \alpha_{\tilde{s}} - \alpha_{\text{H I}} \approx 0.3$. We infer that $\Delta\alpha \neq 0$ could be due to dust emission associated with N_{H_2} .